Data-driven analysis of breathing mode and ion-transit mode in 2D hybrid Hall thruster simulations

Davide Maddaloni*, Adrián Domínguez-Vázquez, and Mario Merino
Equipo de Propulsión Espacial y Plasmas (EP2), Universidad Carlos III de Madrid, Leganés, Spain

Filippo Terragni
Gregorio Millán Institute, Fluid Dynamics, Nanoscience and Industrial Mathematics, and Department of Mathematics, Universidad Carlos III de Madrid, Leganés, Spain

A data-driven modal analysis of low frequency oscillations in a SPT-100-like Hall thruster in the 1–100 kHz range is presented. The used data were generated with a two-dimensional (axial-radial) particle-in-cell (PIC)/fluid simulation code. While proper orthogonal decomposition is unable to uncouple the different dynamics successfully, (higher order) dynamic mode decomposition (HODMD) cleanly isolates the breathing and ion-transit-time modes. Additionally, it facilitates separating transients from the attractors in the data. Thus, the resulting HODMD components can be clustered into two distinct groups with multiple harmonics, enabling the reconstruction of the dynamics of the breathing and ion-transit modes. We show that each plasma variable exhibits a different behavior in each cluster (global oscillations or traveling-wave oscillations), and their amplitudes and frequencies depend on the thruster operating point. This work illustrates the potential of the applied techniques to dissect more complex physics of Hall thrusters and other devices.

I. Introduction

Hall-effect thrusters (HETs) exhibit various types of oscillations over a wide frequency range that affect the discharge current, the plasma properties, and the propulsive performances [1, 2]. While higher-frequency oscillations have been suggested as a mechanism behind anomalous transport, lower-frequency ones also have important consequences on the operation and efficiency of the device [3].

One of the main oscillations characterizing Hall thrusters is the so-called *breathing mode*, which essentially takes place within the chamber along the axial direction. The physical mechanism behind breathing oscillations is currently well understood and it is usually described as a predator-prey type of ionization / neutral-depletion instability [1, 4, 5]. Since in the ionization region the radial magnetic field is strong, the electron mobility is low. If any perturbation increases the local value of the electron density there, the electric field increases in order to keep current continuity. The enhancement of the electric field leads the ionization process to further increase, generating more charges while depleting the neutral population in that region and pushing the ionization front upstream. Since the neutral population is now lower, the ionization rate eventually decreases, and neutrals can reach farther downstream again in order to replenish the channel. The cycle then restarts, delivering a periodic phenomenon taking place usually in the 1-20 kHz range, which is generally well visible in the discharge current.

A second remarkable type of near-axial oscillations in the low-frequency range is the *ion-transit-time oscillation*, so called because it is characterized by periods that are roughly equal to the ion residence time [1, 6, 7]. The prevalent theory of these oscillations links them to an acoustic instability in the ion acceleration region that, by moving upstream, creates an inhomogeneity in the ion velocity profile along the z-axis. For this reason, two populations of ions generate, a slower one, ahead, and a faster one, which follows up, perturbing the potential distribution and eventually leading the two populations to merge. When the two populations merge, the ion current locally exceeds the average current, which may result in a change of sign of the local electric field in order to maintain current continuity. Such type of oscillations usually have a quite broad spectrum between 70-500 kHz.

Isolating and analyzing individual oscillation dynamics and assessing the interrelations between them is essential to provide a better understanding of these phenomena. However, the separation of different behaviors in experimental or numerical data is generally a difficult task, due to the interplay between multiple frequencies, the presence of noise, and

*Email: dmaddalo@pa.uc3m.es.

transient effects. Data-driven analysis techniques can facilitate the uncoupling of the spatial and temporal response of each oscillation/mechanism, without relying on a priori assumptions and avoiding the researcher biases. Among the ample array of analysis tools in this class, modal decomposition techniques offer a valuable insight into the behavior underlying (multidimensional) spatio-temporal data. In particular, proper orthogonal decomposition (POD) [8–10] and dynamic mode decomposition (DMD)-like methods [11, 12] have been successfully used in a variety of applications, such as fluid dynamics [13–15] , acoustics [16], structural vibrations [17, 18], damage detection [19], infectious diseases [20], and fusion plasma [21], to mention some.

Both POD and DMD are snapshot-based techniques that can be used for post-processing either experimental or simulation data, which are decomposed into a set of intrinsic *modes*. POD modes are ordered according to an energy-like norm, enabling the identification of the most energetic spatial patterns and their time evolution, noise filtering, and a low-dimensional reconstruction of the original dataset that retains the dominant physics. POD modes form an orthonormal basis of the linear subspace generated by the snapshots, which facilitates the construction of reduced order models of the underlying dynamics. As a drawback, the associated temporal amplitudes generally exhibit a spread frequency spectrum. On the other hand, DMD expands a spatio-temporal dataset into dynamically relevant modes with a complex-exponential time evolution, identifying the involved frequencies and growth rates. This, among other tasks, allows the separation of transient behaviors from the quasi-stationary oscillations. DMD modes are not necessarily orthogonal among themselves but each of them features a single frequency. Note that standard DMD [11] can be unreliable for strongly non-linear dynamics with large spectral complexity, producing spurious results, for instance with highly noisy experimental data [22]. In order to overcome some of these limitations, higher order dynamic mode decomposition (HODMD) was recently proposed [12] [23] as an enhancement of standard DMD. The aim is to improve the capabilities of the linear model beneath the DMD algorithm of extracting non-linear dynamics out of the data, by enlarging the number of coordinates (i.e., degrees of freedom) via time-lagged snapshots. This allows to achieve a more precise representation of the dynamical properties of the system under study.

In this work, simulation data of a SPT-100 class HET, obtained from a two-dimensional (2D) axisymmetric hybrid particle-in-cell (PIC)/fluid numerical code known as HYPHEN-HET [24, 25], are analyzed using POD and HODMD. The 2D maps of neutral density n_n, plasma density n, electron temperature T_e, plasma potential ϕ, and axial ion current density J_i are investigated to identify the dominant discharge modes. We discuss the limitations of POD in isolating the two dominant oscillation mechanisms present in the simulation data, the breathing mode and the ion-transit-time dynamics, and show how HODMD can appropriately handle this task. Noise and transient behaviors in the simulation data are characterized and removed, while the breathing mode and the ion-transit mode are identified with and reconstructed from 'clusters' of the stable HODMD modes, which enables the investigation of their spatial, frequency, and phase characteristics.

The rest of the paper is structured as follows. Section II presents an abridged account of the simulation procedure and the simulation data used in this study. Section III presents a brief overview of the applied data-driven algorithms while, finally, Sec. IV illustrates the analysis performed and the results achieved. Section V gathers the conclusions of this work.

II. Simulations setup and data overview

The characteristics of the simulation code used to generate the data for this study are detailed in [24–29]. In the following, only a summary of the main aspects is provided.

HYPHEN-HET is a 2D axisymmetric hybrid PIC/fluid, OpenMP-parallelized HET simulator. The dynamics of the quasineutral plasma bulk are simulated by two main modules: the ion module, which follows a Lagrangian approach for simulating the dynamics of the heavy species (i.e., singly- and doubly-charged ions, and neutrals), and the electron module, which considers a magnetized drift-diffusive (inertialess) fluid model for the electron population, including their energy equation. Single ionization rates are obtained from BIAGI database [30], while double ionization rates follow the Drawin model [31]. An additional, anomalous electron collisionality $\nu_t = \alpha_t \omega_{ce}$ is included in the electron momentum equation to phenomenologically represent the effect of plasma turbulence on electron transport [32–34], with α_t a tuning parameter modeling the turbulence level and $\omega_{ce} = eB/m_e$ the electron gyrofrequency. Here a value $\alpha_t = 0.02$ is set in the domain so that the obtained plasma solution is representative of typical SPT-100 HET experimental data in terms of thrust and specific impulse [35, 36].

Each code module employs a different mesh, optimized for its needs: a structured mesh for the ion module and an unstructured, magnetically-aligned mesh for the electron module. Interpolation is used as needed to carry the necessary coupling variables across modules. Lastly, a dedicated sheath module provides the proper boundary conditions for the

Simulation parameter	Units	Nominal case	Off-nominal case
Thruster chamber length, L	cm	2.85	
Thruster chamber inner radius, r_1	cm	3.50	
Thruster chamber outer radius, r_2	cm	5.00	
Near plume region length	cm	8.15	
Near plume region radius	cm	8.10	
PIC mesh number of cells, nodes	-	1464, 1553	
MFAM number of cells, faces	-	4822, 9796	
Cathode location, z, r	cm	3.12, 6.80	
Cathode emission temperature, T_{cat}	eV	3	
Max. $\|\boldsymbol{B}\|$ at the center line	G	242.75	
Location of max. $\|\boldsymbol{B}\|$ at the center line	cm	2.40	
Average $\|\boldsymbol{B}\|$ at the free loss exit plane	G	5.04	
Discharge voltage, V_d	V	300	200
Simulation (PIC) timestep, Δt	s	1.50×10^{-8}	
Total number of simulation steps	-	240000	
Injected Xe velocity	ms^{-1}	300 (sonic)	
Injected Xe temperature	eV	7.35×10^{-2}	
Injected Xe mass flow, $\dot{m}_A$	$\mathrm{mg\,s}^{-1}$	5	

Table 1 Main SPT-100-like HET simulation parameters for the nominal and off-nominal cases. Both simulations are identical but for the discharge voltage V_d.

quasineutral plasma domain, by solving the non-neutral plasma sheaths that develop around the thruster walls, which are treated as thin surfaces. The emission of secondary electrons on the boron nitride walls [37], and the ion recombination and accommodation of neutrals at all walls[24] are also taken into account.

Table 1 lists the thruster dimensions, the considered parameters and the operating conditions for two simulation cases, hereafter referred to as *nominal* and *off-nominal* cases.

Thruster walls are made of dielectric boron nitride. The downstream boundaries are free particle loss and zero current boundaries, while at the axis $r = 0$ symmetry conditions are imposed. A flux of neutral xenon atoms of $\dot{m}_A = 5$ $\mathrm{mg\,s}^{-1}$ is injected with a Maxwellian distribution from the anode wall, upstream in the thruster channel. According to the cathode model presented in [38], the cathode, identified as the reference point for the electric potential, where $\phi = 0$, is represented by a single mesh cell located in the near plume region, indicated by the white round marker in Figure 1, from where 3 eV electrons are injected into the domain. A prescribed discharge voltage V_d is set between the anode wall and the cathode element, which is 300 V for the nominal case and 200 V for the off-nominal case. Lastly, we impose that the net current emitted by the cathode be equal to the current collected at the anode wall at each time step, which gives the discharge current I_d. The resulting time-averaged discharge power in each case is about 1.8 kW and 1 kW for the nominal and off-nominal cases, respectively.

The simulations feature a total of 240000 simulation steps (equivalent to 3.6 ms of real time), in which the obtained discharge current undergoes around 50-60 HET breathing mode cycles. The simulated variables are time-averaged and stored every 20 simulation steps (equivalent to 0.3 μs, which allows to capture physical phenomena featuring dominant frequencies up to ~1.7 MHz) so that, for each simulation case, a total number of 12000 snapshots is available for analysis.

The plasma variables analyzed in this study are the plasma density n, the neutral density n_n, the electron temperature T_e, the plasma potential ϕ, and the ion current density J_i. The time-averaged maps of some plasma properties for the nominal case are shown in Figure 1. The plasma density peaks inside the channel at around 10^{18} m^{-3} and decreases in the plume region as the plasma expands. A secondary peak appears near the thruster, where the annular jet converges. The electron temperature is largest on the magnetic lines near the cathode, where it reaches 30–35 eV. The electrostatic potential decreases axially with the plume expansion. It is noted that neutral density (not shown) is simulated with a lower count of particles per cell to lighten the computational cost, and therefore noise level for this variable is larger than for the rest. As discussed in the next section, this limits the number of modes that can be successfully extracted

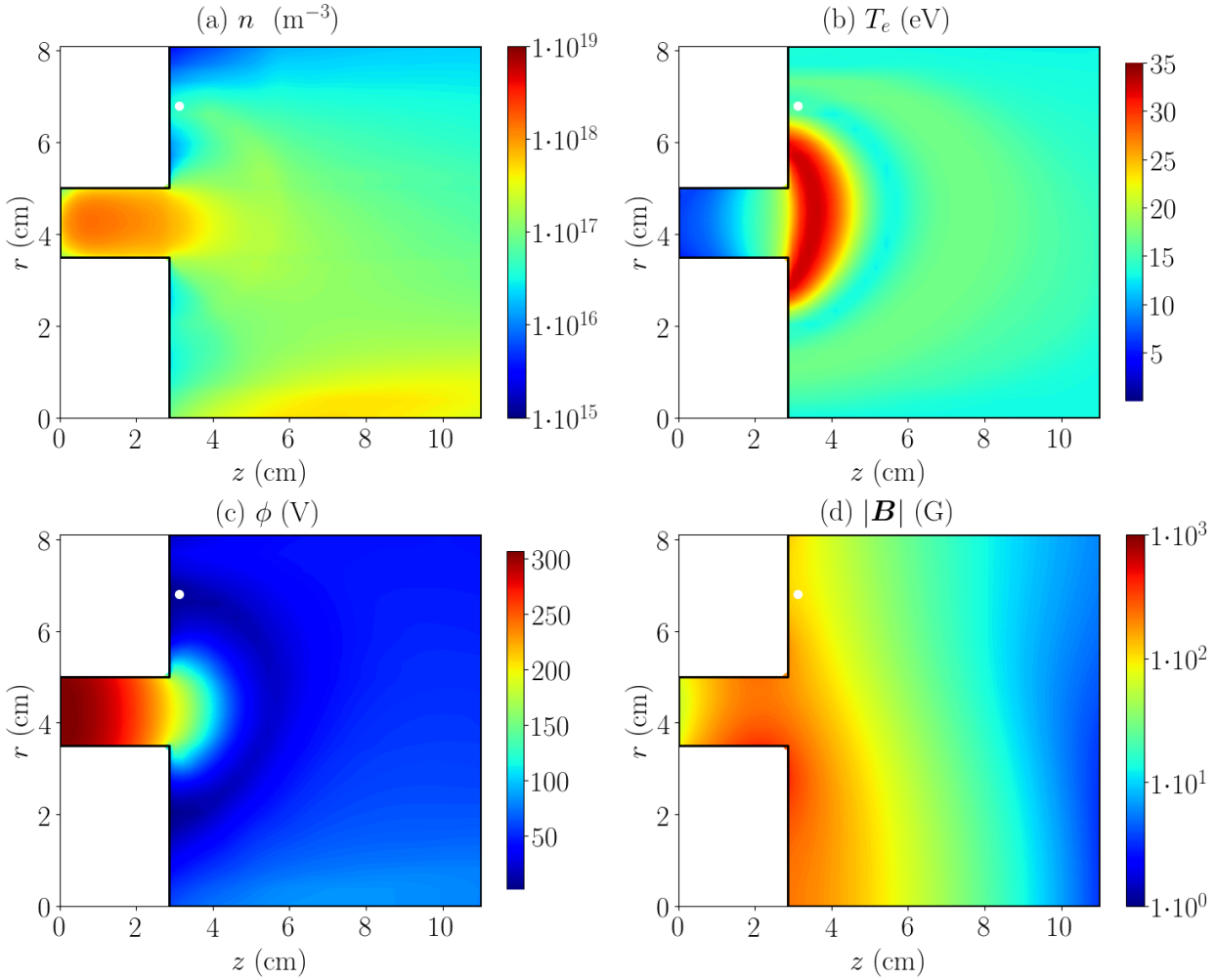

Figure 1 Time-averaged plots of (a) plasma density, (b) electron temperature, and (c) plasma potential. (d) The axial profile of the magnetic field intensity. The white marker, visible on the top of each plot, shows the position in which the cathode is located. For the other variables not shown here, namely ion current density and neutral density, their time-averaged maximum values are respectively 1.17×10^3 **Am**$^{-2}$ **and** 2.88×10^{19} **m**$^{-3}$**.**

from our analysis regarding the neutral density n_n.

The time and frequency response of the discharge current and the plasma density at $z = 0.0515$ m, $r = 0.0406$ m are shown in Figure 2, where their mean values are also reported. As can be observed, the discharge current is dominated by low frequency oscillations near 10^4 Hz (plus its harmonics), corresponding to the breathing mode, which are larger than the mean value. The spectrum has a second, smaller but wider peak at higher frequencies ($\sim 10^5$ Hz), which is related to the ion-transit-time dynamics. The response of the plasma density visibly shares the same features as the discharge current.

III. Data-driven analysis approach

In order to illustrate the data analysis procedure, consider spatio-temporal data given by N real snapshots of dimension M, namely $\boldsymbol{q}_1, \ldots, \boldsymbol{q}_N \in \mathbb{R}^M$. These vectors will store the values of a physical variable $\boldsymbol{q}$ of interest at the M spatial mesh points involved in the numerical simulations,

$$\boldsymbol{q}_n = \boldsymbol{q}(t_n) \quad \text{for } n = 1, \ldots, N, \tag{1}$$

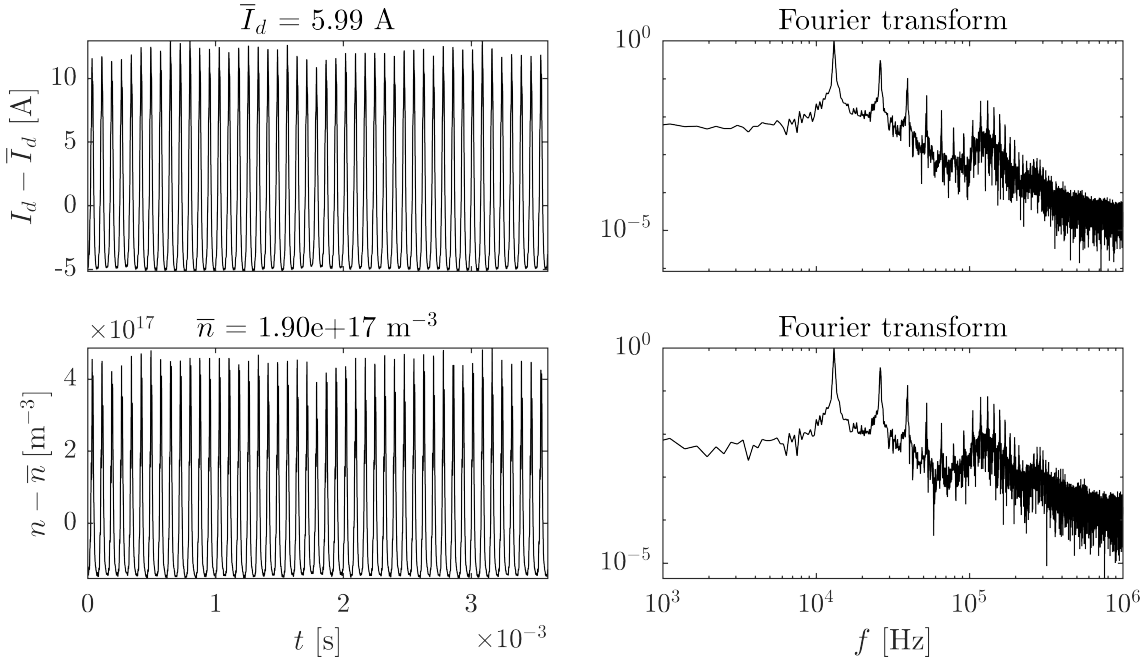

Figure 2 Discharge current (top) and plasma density (bottom) oscillations, for the nominal case, alongside their respective Fourier transforms. Oscillations are non-symmetrical with respect to the zero-axis and have a magnitude of almost three times their mean values, namely 5.99 **A and** $1.90 \cdot 10^{17}$ **m**$^{-3}$**.**

with equally-spaced time instants t_n. Note that the snapshots in equation (1) can be organized as columns of a *snapshot matrix* $\boldsymbol{Q} = [\boldsymbol{q}_1, \boldsymbol{q}_2, \cdots, \boldsymbol{q}_N]$.

A. Proper Orthogonal Decomposition

According to the method of snapshots, standard truncated POD [8, 9] applied to the vectors in equation (1) provides $K < N$ (orthonormal) POD modes, $\boldsymbol{w}_1, \ldots, \boldsymbol{w}_K \in \mathbb{R}^M$, such that each $\boldsymbol{q}_n$ can be approximated as

$$\boldsymbol{q}_n \simeq \sum_{k=1}^{K} \alpha_n^k \boldsymbol{w}_k, \tag{2}$$

where the coefficients α_n^k (POD amplitudes) result from the orthogonal projection of the snapshots onto the linear subspace generated by the modes, namely $\alpha_n^k = \langle \boldsymbol{q}_n, \boldsymbol{w}_k \rangle$. Note that equation (2) yields the best joint root-mean square (RMS) approximation of the snapshots based on K modes, with respect to the considered inner product $\langle \cdot, \cdot \rangle$. Standard POD can be efficiently computed via singular value decomposition (SVD) [39] of the snapshot matrix,

$$\boldsymbol{Q} = \boldsymbol{W} \boldsymbol{\Sigma} \boldsymbol{U}^T, \tag{3}$$

where $\boldsymbol{W}$ ($M \times M$) and $\boldsymbol{U}$ ($N \times N$) are two orthogonal matrices ($\boldsymbol{W}^T \boldsymbol{W} = \boldsymbol{U}^T \boldsymbol{U} = \boldsymbol{I}$), while $\boldsymbol{\Sigma}$ is a sparse $M \times N$ matrix with the singular values σ_k on its main diagonal. Said singular values are non-negative, real, and can be arranged so that $\sigma_1 \geq \sigma_2 \geq \ldots \geq \sigma_r > 0$, being r the rank of $\boldsymbol{Q}$. Note that they are the square roots of the eigenvalues of the correlation matrix $\boldsymbol{Q}^T \boldsymbol{Q}$. Thus, given equation (3), the POD modes are precisely the columns of $\boldsymbol{W}$. Each mode is ranked according to the magnitude of the corresponding singular value, which expresses the energetic content of the mode. To be precise, the term *energy* in this context refers to the Euclidean norm of the data; therefore, the energy associated to each mode is simply the square of the corresponding singular value.

Due to the capability of ranking the modes by energetic importance, POD is widely used for dimension reduction and noise filtering purposes, since it is able to eliminate the smallest and redundant contributions to the data by imposing a truncation on the reconstruction illustrated in equation (2). This is typically done by tuning the amount of left-out energy associated to the modes to be neglected.

Moreover, the frequency response of a POD mode can be extracted from its temporal amplitude by means of the Fourier transform. Hence the decomposition allows to have a closer look at the underlying dominant dynamics, but it still does not provide any strict dynamics isolation, since each mode has a spread spectrum and often mixed frequency contributions to the same mode are present. This happens because of the energy-like norm according to which the mode separation and ranking take place.

B. Higher Order Dynamic Mode Decomposition

DMD-like methods are suitable for the analysis of spatio-temporal data associated with dynamics exhibiting a superposition of time-dependent, exponential growth or decay and oscillations [11]. More precisely, they aim at decomposing each snapshot $\boldsymbol{q}_n$ by an expansion into complex-exponential components of the form

$$\boldsymbol{q}_n \approx \boldsymbol{q}_n^{\mathrm{DMD}} = \sum_{k=1}^{K} a_k \boldsymbol{\psi}_k e^{(\delta_k + i\omega_k)t_n}, \tag{4}$$

being $\boldsymbol{\psi}_k$ complex, normalized (with unit RMS norm) spatial modes, $a_k > 0$ their real amplitudes, ω_k and δ_k their frequencies and growth rates, respectively. Such decomposition, in fact, allows a very specific characterization of each mode and a very neat separation between them, in terms of a single frequency, amplitude, and growth rate.

The dynamical relevance of each mode within the data is represented by its amplitude. On the other hand, according to equation (4), the temporal evolution of the data is divided into a purely oscillating part (terms with negligible growth rates), corresponding to the quasi-steady dynamics or attractor, and decaying/growing contributions (terms with non-negligible growth rates). For the purpose of numerical classification, we consider a mode $\boldsymbol{\psi}_k$ to be quasi-steady when its growth rate multiplied by a timespan equal to five times the breathing characteristic timescale, namely $|5\delta_k t_{br}|$, is smaller than $\ln(2)$. Note that, in a stationary time series, decaying/growing modes are associated with transient processes, which become less relevant as the sampling window of the data becomes longer.

The classic DMD algorithm relies on the so-called *Koopman assumption* [11], according to which a linear mapping is assumed to exist between each snapshot and the next one through the Koopman matrix $\boldsymbol{A}$, so that

$$\boldsymbol{q}_{n+1} = \boldsymbol{A}\boldsymbol{q}_n. \tag{5}$$

Note that equation (5) is not intended to be the actual physical model underlying the data, but a tool leading to an expansion of the form (4). Indeed, once the matrix A is computed (e.g., from the snapshot matrix via the pseudo-inverse), the growth rates and frequencies appearing in equation (4) are related to the nonzero eigenvalues μ_k of A as

$$\delta_k + i\omega_k = \frac{1}{dt}\ln(\mu_k), \tag{6}$$

where dt is the distance between the snapshots. The modes $\boldsymbol{\psi}_k$ are the associated (normalized) eigenvectors. More details can be found in [11, 12]. However, in many real-life applications (including HETs), standard DMD may yield spurious results because of strong non-linearities and noise intrinsic in the data, which leads to a loss of consistency between the assumption (5) and the equation (4).

A way to overcome this limitation consists in introducing the *higher order Koopman assumption* [12] as follows

$$\boldsymbol{q}_{n+d} = \boldsymbol{A}_1\boldsymbol{q}_n + \boldsymbol{A}_2\boldsymbol{q}_{n+1} + \ldots + \boldsymbol{A}_d\boldsymbol{q}_{n+d-1} \quad \text{for } n = 1, 2, \ldots, N-d, \tag{7}$$

with a tunable parameter $d > 1$ that defines time-lagged snapshots to use in the analysis. This has the effect of enlarging the dimension of the problem space in which we seek a linear approximation of the data. We can then rewrite equation (7) as

$$\widetilde{\boldsymbol{q}}_{n+1} = \widetilde{\boldsymbol{A}}\widetilde{\boldsymbol{q}}_n, \tag{8}$$

being

$$\widetilde{\boldsymbol{q}}_n = \begin{bmatrix} \boldsymbol{q}_n \\ \boldsymbol{q}_{n+1} \\ \ldots \\ \boldsymbol{q}_{n+d-2} \\ \boldsymbol{q}_{n+d-1} \end{bmatrix}, \qquad \widetilde{\boldsymbol{A}} = \begin{bmatrix} \boldsymbol{0} & \boldsymbol{I} & \boldsymbol{0} & \ldots & \boldsymbol{0} & \boldsymbol{0} \\ \boldsymbol{0} & \boldsymbol{0} & \boldsymbol{I} & \ldots & \boldsymbol{0} & \boldsymbol{0} \\ \ldots & \ldots & \ldots & \ldots & \ldots & \ldots \\ \boldsymbol{0} & \boldsymbol{0} & \boldsymbol{0} & \ldots & \boldsymbol{I} & \boldsymbol{0} \\ \boldsymbol{A}_1 & \boldsymbol{A}_2 & \boldsymbol{A}_3 & \ldots & \boldsymbol{A}_{d-1} & \boldsymbol{A}_d \end{bmatrix}, \tag{9}$$

where $\widetilde{\boldsymbol{A}}$ is the modified Koopman matrix, while $\boldsymbol{I}$ and $\boldsymbol{0}$ are the $M \times M$ unit and null matrices, respectively. Vectors $\widetilde{\boldsymbol{q}}_n$ are called *modified snapshots* and the resulting *modified snapshot matrix* is indicated by $\widetilde{\boldsymbol{Q}}$.

The procedure to obtain the expansion in equation (4) relying on the assumption in equation (8) is called higher order dynamic mode decomposition (HODMD), which is now briefly summarized following [12]. First, an initial SVD filtering is performed on the original snapshot matrix $\boldsymbol{Q}$ in order to eliminate redundancies and noise. This is accomplished by imposing a threshold on the retained singular values for the reconstruction of the data, namely ε_1. Second, the filtered snapshots are used to build the modified snapshot matrix $\widetilde{\boldsymbol{Q}}$ (by choosing a suitable value for the number d of delayed coordinates), which is also SVD-filtered by means of a second threshold ε_2. Note that, in this work, the two SVD tolerances have been kept the same, namely $\varepsilon_1 = \varepsilon_2 = \varepsilon_{\text{SVD}}$. Then, standard DMD algorithm is applied to the filtered $\widetilde{\boldsymbol{Q}}$, which extracts the modes, growth rates and frequencies in the expansion (4). Finally, the amplitudes are computed via least-squares fitting, and both modes and amplitudes are conveniently rescaled (see [12] for further details).

Among all the modes extracted by the HODMD algorithm, not all of them are kept. Indeed, a filtering of less relevant modes is performed by imposing a relative amplitude tolerance ε_{DMD}, cutting off each mode whose amplitude with respect to the largest one is below the imposed threshold. Moreover, in the present paper, an iterative version of the technique is applied, as in [22]. More precisely, the HODMD algorithm is iterated on the reconstructed data to eliminate spurious modes until achieving convergence of the HODMD spectrum. This last step cleans up the results and provides a neater description of the dominant modes representing the dynamics underlying the data.

The resulting HODMD contributions in equation (4) naturally cluster into groups of similar frequencies, or groups of harmonics of one or more fundamental frequencies. In order to correctly isolate the different dynamics present in the data, this clustering becomes essential, as will be illustrated in the next section.

1. HODMD parameter tuning

As already mentioned, HODMD has some free parameters, consisting of three different thresholds: the reduction tolerance, ε_{SVD}, the amplitude tolerance, ε_{DMD}, and the delayed snapshots number, d. A proper choice of the value of these parameters can play a significant role for a successful HODMD application [23].

In the present work, the reduction tolerance has been chosen requiring that the relative RMS error of the snapshots reconstruction be smaller than ε_{SVD}. Note that this error is easily computed in terms of the singular values using well-known SVD formulae [39]. All analyzed data are expected to have a noise level of at least 1%, which is roughly the simulation accuracy. This means that any SVD/POD mode with singular value smaller than that level should be regarded as noise. For this reason, for each variable, it has been imposed $\varepsilon_{\text{SVD}} = 0.01$, except for the neutral density, for which $\varepsilon_{\text{SVD}} = 0.05$. Indeed, as already mentioned, this is due to the lower precision of this specific variable.

Secondly, the amplitude tolerance has been imposed to be $\varepsilon_{\text{DMD}} = 0.05$ for each variable. This parameter is not critical though and, in fact, this value is generally quite indulgent since it allows a large majority of the modes to be kept.

Finally, the number d of delayed snapshots is the foremost value to be chosen, being the one regulating the ability of HODMD of improving its performance with respect to standard DMD. For this selection, an empirical analysis has been performed, as suggested in [12], in which the relative RMS error of the HODMD reconstructed snapshots as a function of d is inspected to identify an optimal value range. Indeed, the RMS error turned out to exhibit a steep region, in which it decreases when increasing d, and then a plateau region where it is roughly constant. The value of d where this inflection occurs has been selected, being between 300 and 500 depending on the variable. It has also been checked that small variations of d around this value do not strongly affect the outputs, so ascertaining its optimal range in this fashion is deemed generally enough.

The implementation of the HODMD algorithm used in the present work is based on the original code by Le Clainche and Vega [40].

IV. Results and discussion

In this section, we report the independent application of the POD and HODMD techniques described above to each variable in the nominal simulation case. Prior to analysis, the time-average was subtracted from the data. In addition, it has been checked that the simultaneous analysis of all variables, namely processing a single snapshot matrix with all the variables together (after normalizing the snapshots of each one of them by their respective RMS norm), yields nearly identical results.

Figure 3 shows the first six POD modes of the plasma density and electron temperature for the nominal case. The energetic dominance of the first two modes is clear, as their energy norms represent above 95% of the total. These two

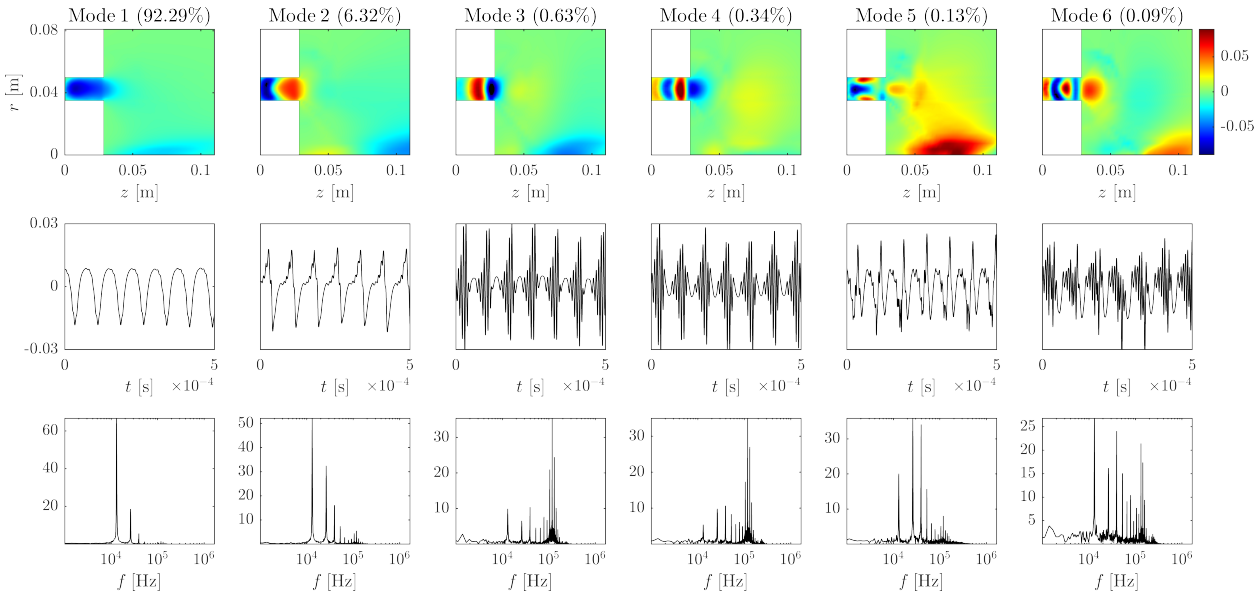

a)

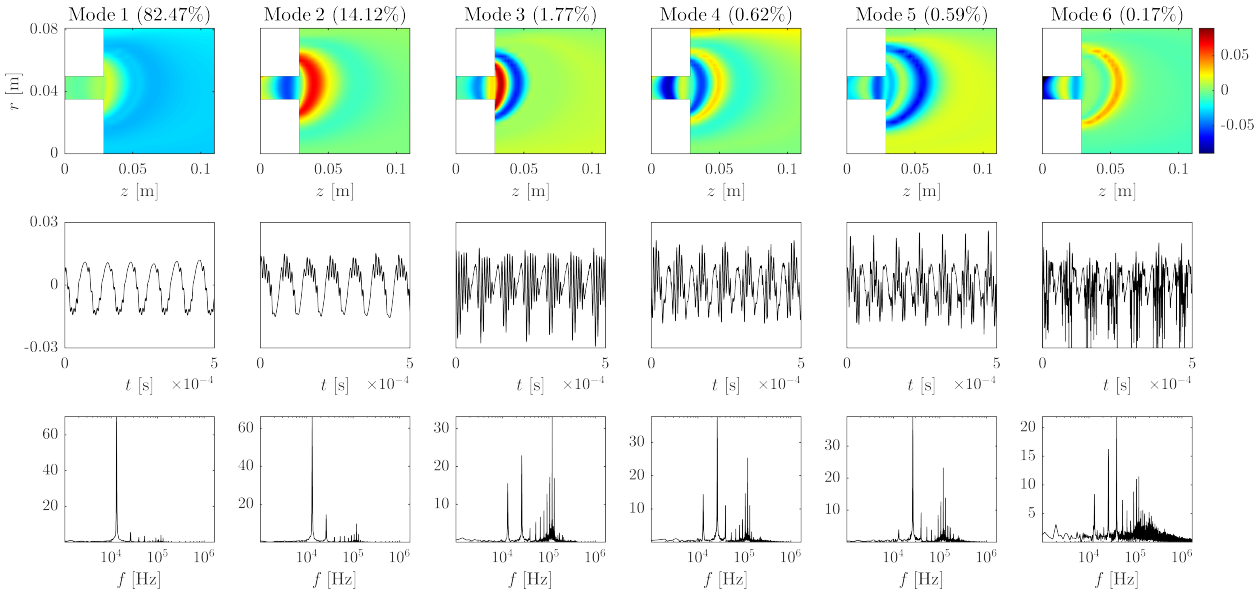

b)

Figure 3 First six dominant POD modes for (a) plasma density and (b) electron temperature, alongside the evolution of the corresponding POD amplitudes in temporal and Fourier domains, for the nominal case. Note that modes and amplitudes are normalized as in standard POD.

modes are easily identified with the breathing mode, in view of their frequency spectrum and spatial shape. The next POD modes, though, show a mixture of frequencies belonging to what are alleged to be different behaviors, covering both the breathing mode range and the ion-transit-time range. Indeed, it can be observed that the fundamental breathing mode frequency is 13.1 kHz. The spectrum of the ion-transit-time dynamics is spread over a range of frequencies around 100–130 kHz. All POD modes with energy content in this frequency range are strongly modulated by the breathing mode frequency.

This illustrates that POD is unable to correctly isolate and separate the two types of oscillatory mechanisms present in the thruster. This is related to the fact that, as previously stated, POD recognizes the most energetically-dominant structures in the data, regardless of their dynamical relevance and frequency content, meaning that strict isolation of single behaviors is generally troublesome.

Amplitude vs. frequency diagrams resulting from the HODMD analysis of the nominal case are displayed on the left side of Figure 4. Plasma density, electron temperature, plasma potential, and ion current density all exhibit a similar amplitude spectrum, consisting of two clear peaks, the first one corresponding to the breathing frequency and the second one to the ion-transit frequency (the figure only shows the first two variables). This two-peak distribution, together with the different spatial behavior of the modes in each group as discussed further below, suggests clustering HODMD modes into 'breathing mode components' (blue circles in the figure) and 'ion-transit-time mode components' (red diamonds in the figure).

The neutral density in Figure 4, on the other hand, shows only the peak associated with the breathing mode and is missing the ion-transit part of the spectrum. This suggests that, while neutrals play a central role in the dynamics of the former, they do not strongly participate in the latter. Nevertheless, as previously stated, neutral density has a lower precision in the performed simulations as a result of an intentionally lower phase space resolution to save computational resources, hence its noise could overshadow any lower-amplitude modes.

As expected, the breathing mode components have a large amplitude in the nominal case, comparable with the peak values of each variable reported in the caption of Figure 1. Between 4–5 components are recovered for all variables, except for the neutral density, which has 2. The ion-transit components have amplitudes that are roughly one order of magnitude lower than the breathing mode ones, for n, T_e, ϕ, and J_i.

All the frequencies are, within the uncertainty present in the data and the method of analysis, harmonics of the frequency of the first breathing mode component, which is 13.1 kHz. Indeed, the main frequency in the ion-transit cluster is found to be 9 times this value, namely 118 kHz. As discussed further down, this is not so in other simulated cases, where two distinct fundamental frequencies (one belonging to the breathing mode, another one to the ion-transit mode) and their respective harmonics are found.

The plots on the right side of Figure 4 display the growth rates of the HODMD modes (multiplied by the breathing characteristic timescale, t_{br}) vs. frequency. The threshold on the growth rates referred to in Section III.B is also displayed. This is used to identify unstable dynamics by classifying as unstable any mode associated with an amplification of twice its initial amplitude after five cycles of the breathing characteristic time. Intermediate iterations of the HODMD algorithm showed additional modes above this threshold, corresponding to noise in the data. But, after convergence, all the retained modes are stable, within the chosen tolerance. Note that, the quasi-steady dynamics of the two identified HET oscillations can be reconstructed by superposing the components in each cluster separately. This is done by means of equation (4) setting to zero the corresponding, small growth rates.

Figure 5 shows the shape of the fundamental HODMD component attributed to the breathing mode, displaying the spatial magnitudes and phase angles for each variable. Two distinct behaviors can be pointed out: while plasma density, neutral density, and ion current density oscillate strongly and mainly inside the thruster channel, electron temperature and plasma potential oscillations occur mainly outside, in the near plume. The oscillations of the electron temperature and electrostatic potential are small in magnitude compared to the time-averaged potential. The phase angle plots also reveal fundamental differences among the variables: while plasma density, neutral density, and ion current density have essentially constant phase throughout the channel mid-radius line, electron temperature and plasma potential clearly show an outward-traveling wave structure. We observe that plasma density and ion current density oscillations are in phase, and that electron temperature and plasma potential oscillations are in phase too. It can also be noted that the neutral density leads by 90 deg the plasma density, which is consistent with the prevailing predator-prey models of the breathing mode [5].

Figure 6 displays the fundamental ion-transit HODMD mode, evidencing a different behavior compared to the breathing mode. Firstly, the oscillations of all variables now take place either inside the channel or at its exit (with the exception of ion current density, whose oscillations extend downstream too). The amplitude of these oscillations is about one order of magnitude smaller than in the breathing mode, as discussed above. Secondly, the traveling wave structure

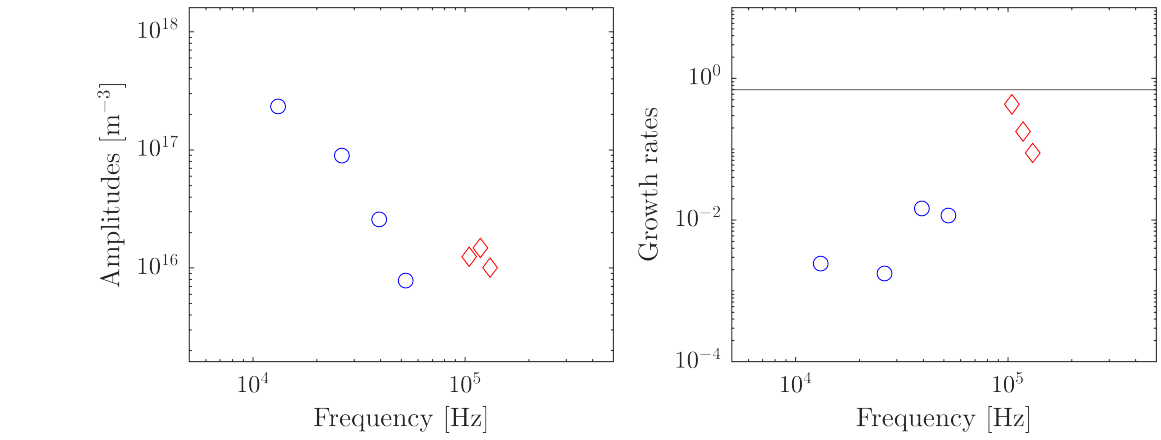

a)

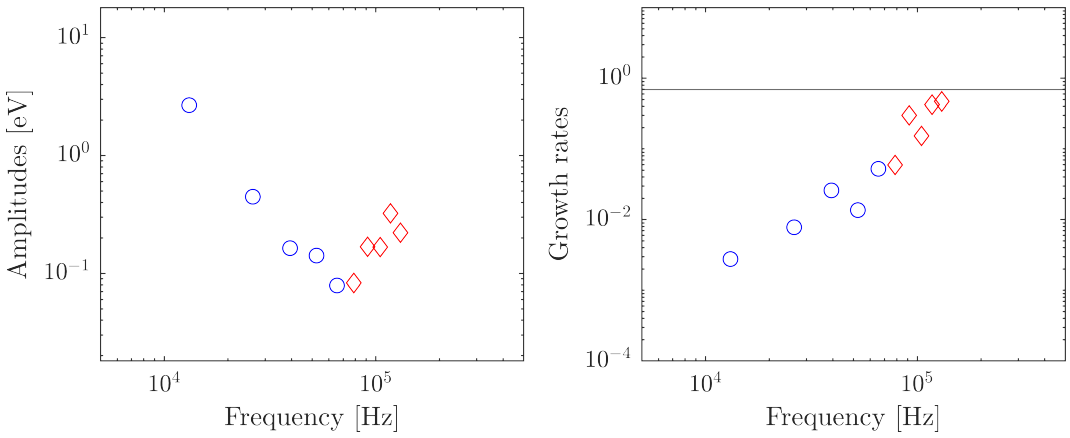

b)

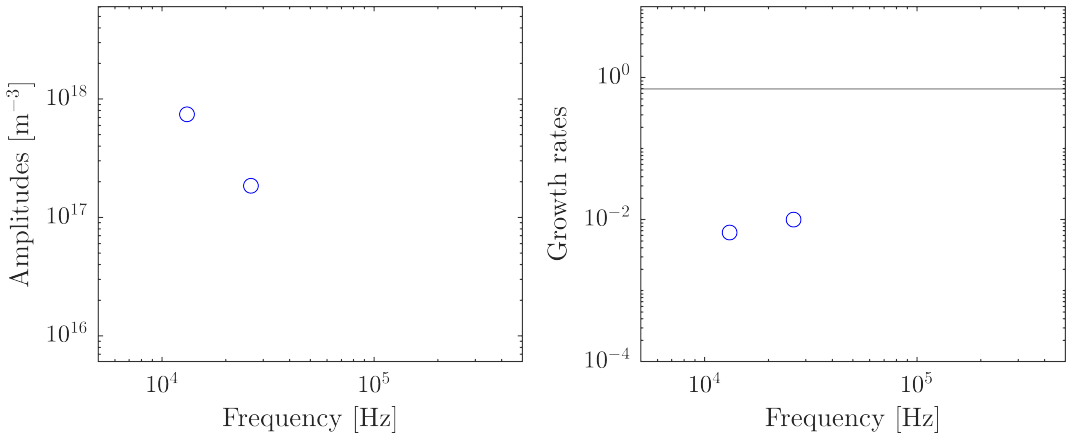

c)

Figure 4 HODMD mode amplitudes and growth rates as a function of frequency for (a) plasma density, (b) electron temperature, and (c) neutral density, for the nominal case. Blue circles are modes belonging to the breathing mode cluster (with fundamental frequency 13.1 **kHz), while red diamonds are modes belonging to the ion-transit cluster (with fundamental frequency** 118 **kHz). Ion current density and plasma potential, which are not reported in this figure, show the same behavior of plasma density and electron temperature, respectively. The amplitude associated with the breathing fundamental frequency, for these last two variables, is equal to** 11.2 **V and** 217 **Am^{-2}, respectively.**

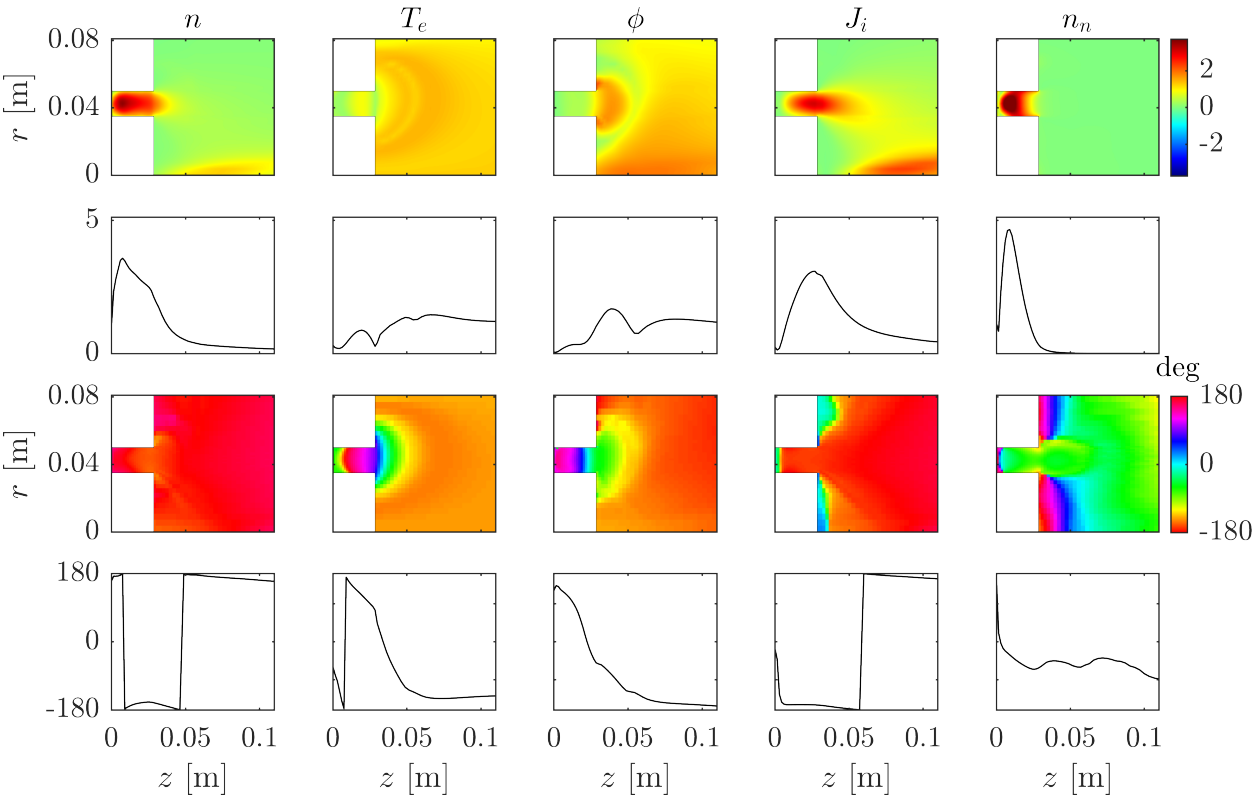

Figure 5 Plasma density, electron temperature, plasma potential, ion current density, and neutral density in terms of the fundamental HODMD mode in the breathing mode cluster, for the nominal case (with frequency 13.1 **kHz). The first two rows depict the magnitude of the mode for each variable, in the 2D domain and along the** r = 0.0406 **m line, respectively. Correspondingly, the last two rows show the phase angle of the mode.**

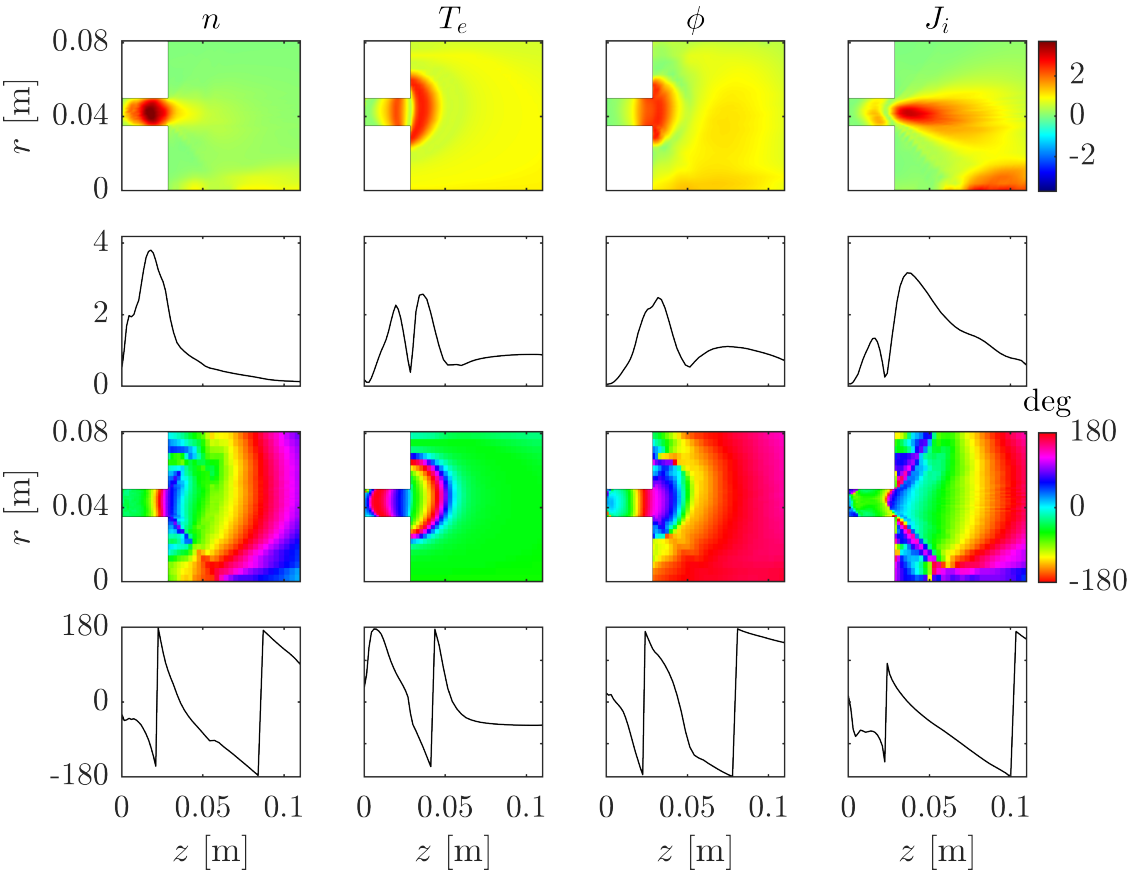

Figure 6 Plasma density, electron temperature, plasma potential, and ion current density in terms of the fundamental HODMD mode in the ion-transit cluster, for the nominal case (with frequency 118 kHz). Each row of plots has the same description as in Figure 5.

is now present in all variables and, furthermore, the associated axial wavenumber is larger than in the breathing mode. Finally, as previously mentioned, the transit-time oscillations are called so due to their relation with the ion residence characteristic timescale, $u_i/L = 1/\tau \approx f_{itt}$. Computing the mean ion velocity approximately in the acceleration region of the plume and dividing it by its axial length, $f_{itt} = 127$ kHz is obtained, which is directly comparable with the HODMD frequency of the fundamental ion-transit mode component, namely 118 kHz. Indeed, there is also a good correspondence between the axial phase velocity and the mean ion velocity for this mode, equal to 1252 ms^{-1} and 1497 ms^{-1}, respectively.

It has been checked that these features are present, correspondingly, in all components of the breathing mode cluster and all components of the ion-transit cluster, providing additional support for the separation between them.

In order to complete the analysis, we next inspect the off-nominal simulation case, to explore how the identified behaviors change when the discharge voltage is varied from 300 V to 200 V. The mean discharge current decreases from 5.99 A to 5.23 A, while the mean plasma density sees a slight increment from 1.90×10^{17} m^{-3} to 2.17×10^{17} m^{-3}. Moreover, the amplitude of the oscillations of the discharge current and plasma density is now smaller (roughly equal to said mean values, rather than about three times as in the nominal case). This is already suggesting that, since these oscillations essentially represent the breathing mode dynamics, the strength of the latter decreases with a decreasing discharge voltage.

One explanation to this change of relative importance can be found in the fact that lowering the discharge voltage (i.e., the input power) inevitably affects the ionization rate, causing it to decrease significantly. Indeed, being the breathing mode essentially related to the ionization mechanism, a decrease in the ionization rate induces a decrease in the oscillations magnitude as well, as previously pointed out. On the other hand, being the ion-transit mode an acoustic-related dynamics, it gets essentially unaffected by the input power and its absolute importance in the phenomenon goes unchanged.

The POD modes of this simulation (not shown) reproduce the general trends described so far for the nominal case, although now even the first, most energetic modes exhibit a mixture of the breathing frequency and the ion-transit spectrum. This basically means that the loss of the breathing mode dominance is reflected on the energetic side too.

As in the nominal case, n, T_e, ϕ, and J_i exhibit comparable behaviors, and the spatial structure of the HODMD mode components is qualitatively unaffected. This implies that decreasing the discharge voltage does not change much the underlying mechanisms of these oscillations, beyond the aforementioned modulation of their amplitudes. In this regard, Figure 7 shows the diagrams of amplitudes vs. frequencies and growth rates vs. frequencies extracted by means of HODMD for the off-nominal case. Now, the breathing mode main frequency corresponds to 10.8 kHz, while the ion-transit one corresponds to 112 kHz.

The relative importance of the breathing and ion-transit clusters is now comparable, as the breathing mode amplitudes have decreased. Some of the previously visible harmonics of the breathing mode are lost but, on the other hand, the first harmonic of the ion-transit mode can now be recovered, in the 200–300 kHz range. Likewise, a small-amplitude component in the ion-transit frequency range is also recovered for the neutral density n_n.

In this off-nominal case, the breathing mode and the ion-transit mode have clearly separated fundamental frequencies, which are not multiples of each other, with a ratio of roughly 10.35. Hybrid harmonics of the two frequencies and a much richer component content of the ion-transit cluster are also visible in the results.

V. Conclusions

Low frequency axial-radial oscillations in the plume of a SPT-100-like Hall thruster have been investigated for two different operational conditions by means of data-driven techniques, namely POD and HODMD, using the simulation data of a 2D axisymmetric hybrid PIC/fluid code (HYPHEN-HET).

While POD can only establish an energy-norm decomposition of the data, useful for noise filtering and dimensionality reduction, the technique is unable to isolate the dynamics of different oscillation mechanisms present in the data. HODMD, on the other hand, achieves this separation by representing the data as a superposition of single-frequency, but non-orthogonal modes. The HODMD algorithm goes beyond standard DMD in the study of nonlinear systems, by enlarging the coordinate space using time-lagged snapshots.

The analysis has permitted isolating and reconstructing the breathing mode dynamics, observing the strong global oscillations inside the channel of the plasma density and the neutral density that correspond well to the expectations of predator-prey models. In addition, it allowed to identify an associated traveling wave structure in the electron temperature and the electrostatic potential. The HODMD spectrum shows a cluster of components that are harmonics of

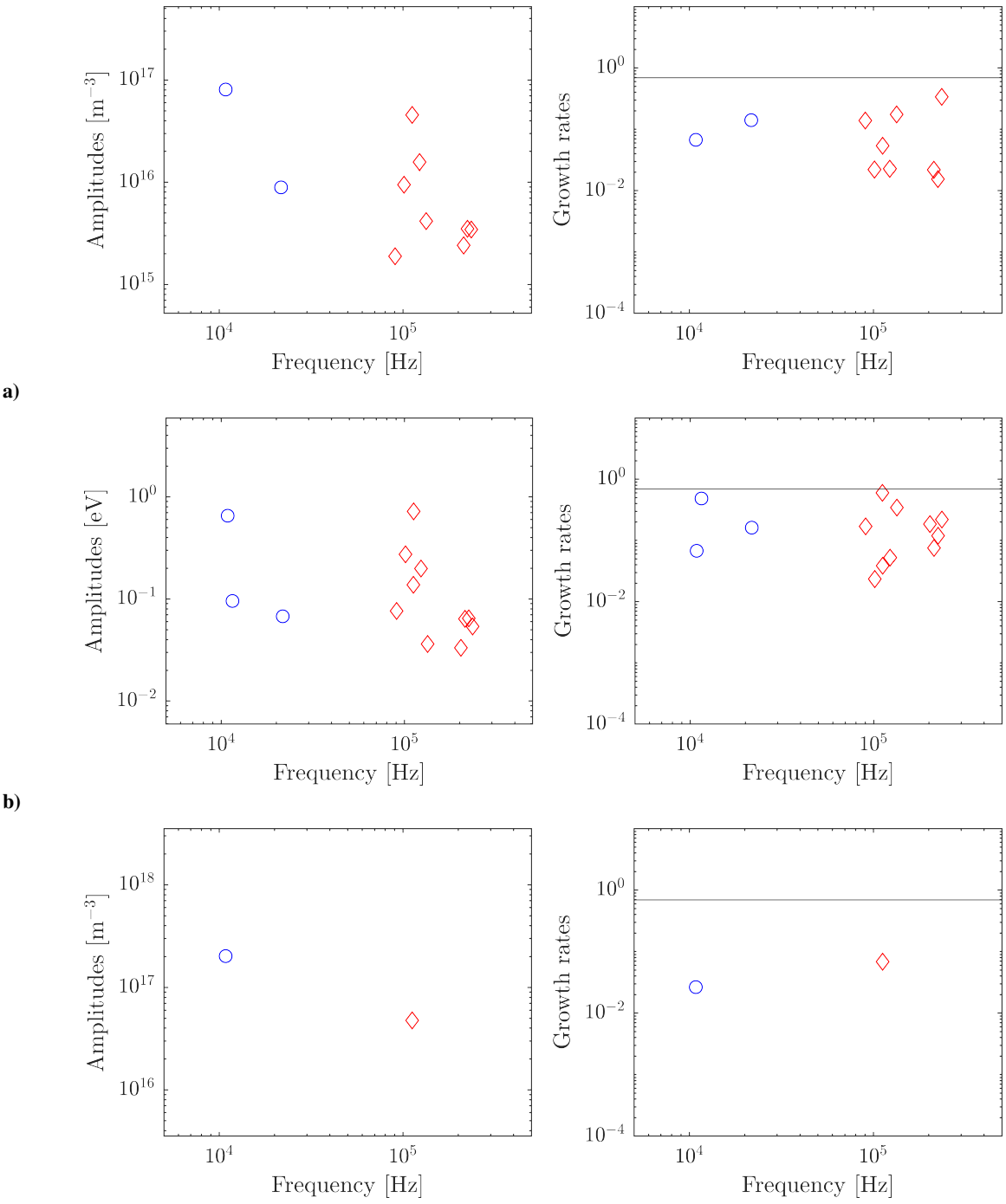

Figure 7 HODMD mode amplitudes and growth rates as a function of frequency for (a) plasma density, (b) electron temperature, and (c) neutral density, for the off-nominal case. Blue circles are modes belonging to the breathing mode cluster (with fundamental frequency 10.8 kHz), while red diamonds are modes belonging to the ion-transit cluster (with fundamental frequency 112 kHz). Ion current density and plasma potential, not reported in this figure, show the same behavior of plasma density and electron temperature, respectively. The amplitude associated with the breathing fundamental frequency, for these last two variables, is equal to 2.16 V and 66.1 Am^{-2}, respectively.

the fundamental breathing frequency.

Likewise, smaller oscillations were found in the ion-transit frequency range, corresponding to the ion residence time in the acceleration region of the thruster. These oscillations exhibit traveling wave structures for all variables, except for the neutral density that is essentially not excited by them and does not play an important role in their physics.

Traveling waves in either mode are essentially axial, with a local wavenumber that can be directly estimated from the results.

The comparison between the two simulation cases has shown that, by decreasing the discharge voltage, the oscillation frequencies shift and the fundamental frequencies of the breathing mode and ion-transit mode become clearly non-commensurable. At the same time, the amplitude of the breathing mode oscillations decreases, becoming comparable to that of the ion-transit dynamics.

This work has illustrated the potential and suitability of data-driven techniques to the analysis of oscillations in electric propulsion systems, which are applicable to either experimental measurements or simulation data. In particular, apart from the quite well-known POD, the major focus has been on HODMD, which has the advantage to allow isolating and individually characterizing the investigated dynamics, since it associates one single frequency, growth rate, and amplitude to each extracted mode. The analysis also provides a clear estimate of the noise level in the data, thus enabling to filter out numerical errors and non-physical perturbations. Hence, noise-free dynamics can be reconstructed for each separate oscillation or mechanism present in the data. Further work will extend this analysis to additional operation points to complement the parametric study.

Acknowledgments

This work has been supported by the Madrid Government (Comunidad de Madrid) under the Multiannual Agreement with UC3M in the line of "Fostering Young Doctors Research" (MARETERRA-CM-UC3M), and in the context of the V PRICIT (Regional Programme of Research and Technological Innovation.

References

[1] Choueiri, E., "Plasma oscillations in Hall thrusters," *Physics of Plasmas*, Vol. 8, No. 4, 2001, pp. 1411–1426.

[2] Ahedo, E., "Plasmas for space propulsion," *Plasma Physics and Controlled Fusion*, Vol. 53, No. 12, 2011, p. 124037. URL `http://stacks.iop.org/0741-3335/53/i=12/a=124037`.

[3] Kaganovich, I. D., Smolyakov, A., Raitses, Y., Ahedo, E., Mikellides, I. G., Jorns, B., Taccogna, F., Gueroult, R., Tsikata, S., Bourdon, A., Boeuf, J.-P., Keidar, M., Powis, A. T., Merino, M., Cappelli, M., Hara, K., Carlsson, J. A., Fisch, N. J., Chabert, P., Schweigert, I., Lafleur, T., Matyash, K., Khrabrov, A. V., Boswell, R. W., and Fruchtman, A., "Perspectives on Physics of ExB Discharges Relevant to Plasma Propulsion and Similar Technologies," *Physics of Plasmas*, Vol. 27, No. 12, 2020, p. 120601. https://doi.org/10.1063/5.0010135.

[4] Albarede, L., Mazouffre, S., Bouchoule, A., and Dudeck, M., "Low-frequency electron dynamics in the near field of a Hall effect thruster," *Physics of Plasmas*, Vol. 13, 2006, p. 063505.

[5] Barral, S., and Ahedo, E., "Low-frequency model of breathing oscillations in Hall discharges," *Physical Review E*, Vol. 79, 2009, p. 046401.

[6] Bareilles, J., Hagelaar, G., Garrigues, L., Boniface, C., Boeuf, J., and Gascon, N., "Critical assessment of a two-dimensional hybrid Hall thruster model: Comparisons with experiments," *Physics of Plasmas*, Vol. 11, No. 6, 2004, pp. 3035–3046.

[7] Barral, S., Makowski, K., Peradzynski, Z., and Dudeck, M., "Transit-time instability in Hall thrusters," *Physics of Plasmas*, Vol. 12, 2005, p. 073504.

[8] Sirovich, L., "Turbulence and the dynamics of coherent structures," *Q. Appl. Math.*, Vol. XLV, 1987, pp. 561–590.

[9] Chatterjee, A., "An introduction to the proper orthogonal decomposition," *Current Science*, Vol. 78, 2000, pp. 808–817.

[10] Kosambi, D., "Statistics in function space," *DD Kosambi*, Springer, 2016, pp. 115–123.

[11] Schmid, P. J., "Dynamic mode decomposition of numerical and experimental data," *Journal of fluid mechanics*, Vol. 656, 2010, pp. 5–28.

[12] LeClainche, S., and Vega, J. M., "Higher order dynamic mode decomposition," *SIAM J. Appl. Dyn. Syst.*, Vol. 16, 2017, pp. 882–925.

[13] Holmes, P., Lumley, J. L., Berkooz, G., and Rowley, C. W., *Turbulence, coherent structures, dynamical systems and symmetry*, Cambridge University Press, 2012.

[14] Stegeman, P., Ooi, A., and Soria, J., "Proper orthogonal decomposition and dynamic mode decomposition of under-expanded free-jets with varying nozzle pressure ratios," *Instability and Control of Massively Separated Flows*, Springer, 2015, pp. 85–90.

[15] Taira, K., Brunton, S. L., Dawson, S. T. M., Rowley, C. W., Colonius, T., McKeon, B. J., Schmidt, O. T., Gordeyev, S., Theofilis, V., and Ukeiley, L. S., "Modal analysis of fluid flows: an overview," *AIAA Journal*, Vol. 55, 2017, pp. 4013–4041.

[16] Jourdain, G., Eriksson, L.-E., Kim, S. H., and Sohn, C. H., "Application of dynamic mode decomposition to acoustic-modes identification and damping in a 3-dimensional chamber with baffled injectors," *Journal of Sound and Vibration*, Vol. 332, No. 18, 2013, pp. 4308–4323.

[17] Cusumano, J., Sharkady, M., and Kimble, B., "Experimental measurements of dimensionality and spatial coherence in the dynamics of a flexible-beam impact oscillator," *Philosophical Transactions of the Royal Society of London. Series A: Physical and Engineering Sciences*, Vol. 347, No. 1683, 1994, pp. 421–438.

[18] Feeny, B., and Kappagantu, R., "On the physical interpretation of proper orthogonal modes in vibrations," *Journal of sound and vibration*, Vol. 211, No. 4, 1998, pp. 607–616.

[19] Ruotolo, R., and Surace, C., "Using SVD to detect damage in structures with different operational conditions," *Journal of sound and vibration*, Vol. 226, No. 3, 1999, pp. 425–439.

[20] Proctor, J. L., and Eckhoff, P. A., "Discovering dynamic patterns from infectious disease data using dynamic mode decomposition," *International health*, Vol. 7, No. 2, 2015, pp. 139–145.

[21] van Milligen, B. P., Sánchez, E., Alonso, A., Pedrosa, M. A., Hidalgo, C., Martín de Aguilera, A., and López Fraguas, A., "The use of the biorthogonal decomposition for the identification of zonal flows at TJ-II," *Plasma Phys. Control. Fusion*, Vol. 57, 2015, p. 025005.

[22] Le Clainche, S., Vega, J. M., and Soria, J., "Higher order dynamic mode decomposition of noisy experimental data: The flow structure of a zero-net-mass-flux jet," *Experimental Thermal and Fluid Science*, Vol. 88, 2017, pp. 336–353.

[23] Vega, J. M., and Le Clainche, S., *Higher order dynamic mode decomposition and its applications*, Academic Press, 2020.

[24] Domínguez-Vázquez, A., "Axisymmetric simulation codes for Hall effect thrusters and plasma plumes," Ph.D. thesis, Universidad Carlos III de Madrid, Leganés, Spain, 2019.

[25] Domínguez-Vázquez, A., Zhou, J., Fajardo, P., and Ahedo, E., "Analysis of the plasma discharge in a Hall thruster via a hybrid 2D code," 36^{th} *International Electric Propulsion Conference*, Electric Rocket Propulsion Society, Vienna, Austria, 2019.

[26] Domínguez, A., Pérez-Grande, D., Fajardo, P., and Ahedo, E., "NOMADS: Development of a versatile plasma discharge simulation platform for electric propulsion," *Space Propulsion Conference 2016*, Association Aéronautique et Astronautique de France, Rome, Italy, May 2-6, 2016.

[27] Domínguez-Vázquez, A., Cichocki, F., Merino, M., Fajardo, P., and Ahedo, E., "2D and 3D Hybrid PIC/Fluid Modelling of Electric Thruster Plumes," 35^{th} *International Electric Propulsion Conference*, Electric Rocket Propulsion Society, Atlanta, GA, 2017.

[28] Cichocki, F., Domínguez-Vázquez, A., Merino, M., and Ahedo, E., "Hybrid 3D model for the interaction of plasma thruster plumes with nearby objects," *Plasma Sources Science and Technology*, Vol. 26, No. 12, 2017, p. 125008.

[29] Domínguez-Vázquez, A., Cichocki, F., Merino, M., Fajardo, P., and Ahedo, E., "Axisymmetric plasma plume characterization with 2D and 3D particle codes," *Plasma Sources Science and Technology*, Vol. 27, No. 10, 2018, p. 104009. https://doi.org/10.1088/1361-6595/aae702.

[30] Stephen Francis Biagi, "Cross sections extracted from PROGRAM MAGBOLTZ, VERSION 7.1 JUNE 2004," , June 2004. URL www.lxcat.net/Biagi-v7.1, [Online; accessed 5-July-2021].

[31] Mitchner, M., and Kruger Jr., C., *Partially ionized gases*, John Wiley and Sons, Hoboken, NJ, 1973.

[32] Boeuf, J., and Garrigues, L., "Low frequency oscillations in a stationary plasma thruster," *J. Applied Physics*, Vol. 84, No. 7, 1998, pp. 3541–3554.

[33] Fife, J., "Hybrid-PIC Modeling and Electrostatic Probe Survey of Hall Thrusters," Ph.D. thesis, Massachusetts Institute of Technology, 1998.

[34] Parra, F., Ahedo, E., Fife, M., and Martínez-Sánchez, M., "A two-dimensional hybrid model of the Hall thruster discharge," *Journal of Applied Physics*, Vol. 100, 2006, p. 023304.

[35] Sankovic, J., Hamley, J., and Hang, T., "Performance evaluation of the russian SPT-100 thruster at NASA LeRC," *23rd International Electric Propulsion Conference, Seattle, WA*, 1993.

[36] Mazouffre, S., Echegut, P., and Dudeck, M., "A calibrated infrared imaging study on the steady state thermal behaviour of Hall effect thrusters," *Plasma Sources Science and Technology*, Vol. 16, No. 1, 2006, p. 13.

[37] Ahedo, E., and Pablo, V. d., "Combined effects of electron partial thermalization and secondary emission in Hall thruster discharges," *Physics of Plasmas*, Vol. 14, 2007, p. 083501.

[38] Maqueda, I., Escobar, D., and Ahedo, E., "Advances on a Hall thruster hybrid code," *30th International Electric Propulsion Conference, Florence, Italy*, 2007.

[39] Golub, G. H., and van Loan, G. T., *Matrix computations*, John Hopkins Univ. Press, 1996.

[40] https://github.com/LeClaincheVega/HODMD, 2017.